Profilometry of toroidal surfaces with an improved Ronchi test

Santiago Royo, Josep Arasa, and Carles Pizarro

An implementation of the well-known Ronchi test technique, which allows for the profilometric measurement of nonrotationally symmetrical surfaces, is presented and applied to the measurement of toroidal surfaces. Both the experimental setup and the data-processing procedures are described, and parameters such as the radius of curvature of the sample surface, the orientation of its principal meridians, and the position of its vertex are measured by means of the values of the local normal to the surface obtained at a set of sampling points. Integration of these local normal values allows for the reconstruction of the three-dimensional profile of the toroidal surface considered with micrometric accuracy, and submicrometric surface details may be calculated by use of surface-fitting procedures. The density of sampling points on the surface may be tailored to fit test requirements, within certain limits that depend on selection of experimental setup.

OCIS codes: 120.6650, 120.4630, 120.4800, 120.3930, 120.4290.

1. Introduction

A variety of techniques are now available for profiling optical-quality surfaces. The Ronchi test has been described as a common quality-assessment tool in the optical shop.[1] It is unable to achieve the accuracy of interferometric techniques, but when used as a deflectometric technique, it has a height measurement range far greater than those of interferometers.[2] This large dynamic range allows the technique to perform profile measurements without the need for *a priori* knowledge of the shape of the measured surface profile, even in the case of nonspherical surfaces. Corrections to the measured values calculated from an expected surface shape are not required. The technique is the subject of active research,[3–8] and it has found applications from intraocular lenses[9] to thermocapillary flow studies under microgravity conditions,[10] among others. Phase-shifting techniques have also been successfully applied[11,12] to several Ronchi test arrangements, although they present the intrinsic problem of the diffractive noise caused in the ronchigrams by the ruling.

Despite its many applications, techniques based on the Ronchi test have been applied, to our knowledge, only to rotationally symmetrical surfaces.[12–14] Incidentally, nonrotationally symmetrical surfaces, such as toroidal or spline surfaces, are becoming increasingly important in many fields of optics, from ophthalmic lenses to the design of optical instrumentation, so there is a growing interest in the development of testing methods for these types of surfaces. In this paper we present an approach to the Ronchi test that, taking advantage of diode laser sources, encoder motors, and computing power, allows for repetitive and reliable measurements of nonrotationally symmetrical surfaces. The presented technique is applied to the measurement of a toroidal sample surface in four different orientations, showing how radius-of-curvature values, the orientation of the surface, and the position of its vertex are reliably measured regardless of how the sample surface is oriented.

The paper is divided into four sections plus the present introduction. In Section 2 we briefly introduce the geometric features of the toroidal surface and the spherocylindrical surface, which will be used throughout the remaining sections of the paper. In Section 3 we provide a short description of the measurement method, depicting the experimental setup used (Subsection 3.A) and describing the data-processing operations that lead us from the measured data to the final surface profile and to the measurement of the parameters of the surface (Subsection

The authors are with the Center for Development of Sensors, Instrumentation and Systems (CD6), Technical University of Catalonia, Violinista Vellsolà 37, E-08222 Terrassa, Spain. S. Royo's e-mail address is royo@oo.upc.es.

Received 3 April 2000; revised manuscript received 27 July 2000.
0003-6935/00/315721-11$15.00/0

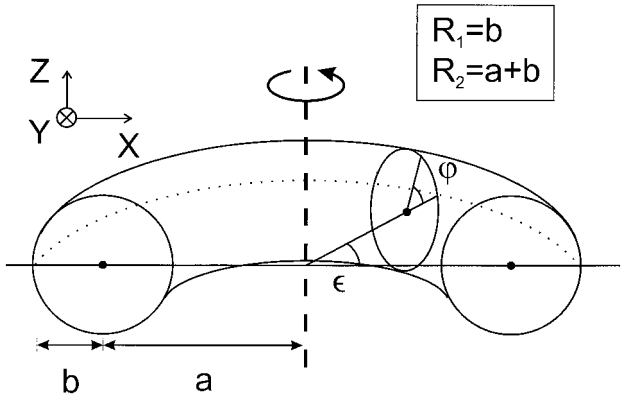

Fig. 1. Toroidal surface and the parameters used for its mathematical description.

3.B). An enhancement technique allowing the user to tailor the density of sampled points on the surface within certain limits is also presented (Subsection 3.C). Section 4 presents experimental results for a measured toroidal surface, starting with a brief description of the experiment performed and the sample used (Subsection 4.A). In Subsection 4.B some intermediate results of the data-processing procedures are presented for a given orientation to provide a better understanding of the measurement technique. Finally, measurement results for three additional orientations of the toroidal sample surface are presented and discussed. Section 5 draws the main conclusions of the study.

2. Geometric Description of the Toroidal Surface

Toroidal surfaces are obtained as the result of the revolution of a circle along an axis that does not cross the center of the circle and that is contained in the same plane of the circle (Fig. 1). If we consider sections of the surface generated by planes containing the shortest line going from the revolution axis to the apex of the surface, the toroidal surface presents only two circular sections: one with the circle's radius of curvature ($R_1 = b$ in Fig. 1) and another one, placed orthogonally, with a radius of curvature given by the circle's radius plus the distance from the center of the circle to the revolution axis ($R_2 = a + b$).

These two orthogonal circular sections will henceforth be called the principal meridians of the surface, following the usual convention in ophthalmic optics. The apex point of the toroidal surface where the two principal meridians intersect is called the vertex of the surface. The same ophthalmic optics convention denotes the meridian with the largest radius as the base curve and the meridian with the smallest one as the cross curve of the toroidal surface.[15]

A parametric description of the toroidal surface in a cylindrical reference system may be written as

$$\begin{aligned} x &= (a + b\cos\phi)\cos\epsilon, \\ y &= (a + b\cos\phi)\sin\epsilon, \\ z &= b\sin\phi, \end{aligned} \tag{1}$$

with the parameters presented in Fig. 1. However, a nonparametric description of the toroidal surface in a rectangular reference system is quite complex and requires an expression dependent on the spatial region considered. This prevents such surfaces from being described as a unique $z = f(x, y)$ expression valid in all space, which would be desirable for three dimensionally to fit a toroidal surface to measured data values in a simple way.

Spherocylindrical surfaces have been shown to be good approximations to toroidal surfaces with the same radii, on the condition that the region considered stay close to the vertex of the surface.[16] The spherocylindrical surface contains two orthogonal circular sections with a maximum and a minimum radius value, which are equivalent to the principal meridians of the toroidal surface. In contrast to the toroidal surface, the transition between those two circular sections are additional circular sections with their radii varying continuously from the maximum to the minimum radius value of the surface. When the maximum and the minimum radius values are oriented along the X and the Y axes, the spherocylindrical surface is mathematically described as

$$z = \frac{x^2/R_1 + y^2/R_2}{1 + \left[1 - \dfrac{(x^2/R_1 + y^2/R_2)^2}{x^2 + y^2}\right]^{1/2}}, \tag{2}$$

R_1 (R_2) being the radius of curvature along the X (Y) axis.

In our measurements spherocylindrical surfaces will be three-dimensionally fitted to the measured profile of the toroidal surface to fix the parameters of the sample surface. With the radius values and the measured areas of the toroidal surface, which will be used throughout the following sections, the spherocylindrical surface may be considered to be fully equivalent to the toroidal surface,[17] so Eq. (3) may be properly fitted to a measured toroidal profile. However, since the principal meridians of the toroidal surface are likely to be tilted and decentered from the X and the Y axes, the general expression of the spherocylindrical surface to be fitted to the measured data is

$$\begin{aligned} x - x_0 &= x_S\cos\theta + y_S\sin\theta, \\ y - y_0 &= -x_S\sin\theta + y_S\cos\theta, \\ z &= \frac{(x - x_0)^2/R_1 + (y - y_0)^2/R_2}{1 + \left\{1 - \dfrac{[(x - x_0)^2/R_1 + (y - y_0)^2/R_2]^2}{(x - x_0)^2 + (y - y_0)^2}\right\}^{1/2}}, \end{aligned} \tag{3}$$

where x_s and y_s are the coordinates of the measured data point, θ is the angle formed by R_1 with the X axis, and (x_0, y_0) is the position of the vertex of the surface. R_1 and R_2 are the radii of curvature of the principal meridians of the surface, being the base or the cross curve depending on how the surface has been positioned. Note that this is not a parametric

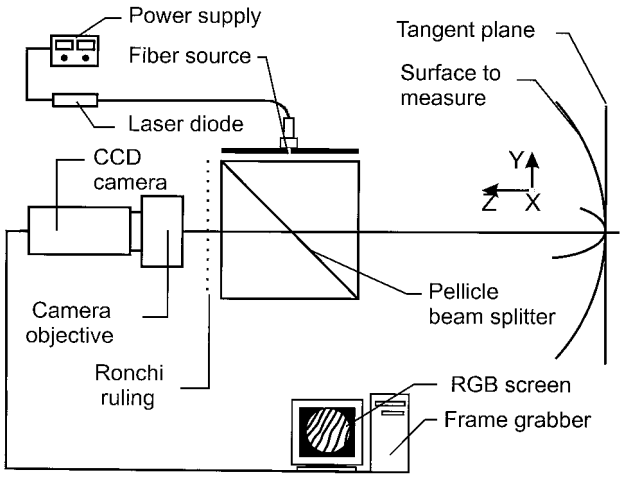

Fig. 2. Experimental setup. RGB: red, green, blue.

equation but a $z = f(x, y)$ expression valid in all space.

3. Measurement Method

A. Experimental Setup

The measurements will be performed in an experimental setup based on the Ronchi test principle, schematically depicted in Fig. 2. A laser diode (wavelength, 635 nm; output power, 3 mW) coupled to an optical fiber with a 4-μm-diameter core is used as a precisely located source. This provides us with a diverging light fan coming from a quasi-point source. This fan impinges on a 100-mm-diameter pellicle beam splitter, which directs the light along an axis containing the surface being tested and the Ronchi ruling. This axis will henceforth be called the Z axis, and its origin is considered to be located at the vertex of the surface being measured, with its positive values increasing in the direction of the Ronchi ruling. The X and the Y axes are defined consistently in the directions shown in Fig. 2.

The redirected light fan impinges on the sample surface and is reflected toward the Ronchi ruling, formed by a pattern of dark and light stripes of equal size. The surface has been arranged to stay with the tangent plane at its vertex parallel to the defined XY plane, and it has been centered manually. A set of four different orientations of the surface may be achieved by rotation of its mount in 30° steps. These orientations are called G00, G30, G60, and G90, assuming in the G00 orientation that the base curve of the sample surface is oriented along the X axis and that, after three consecutive rotations yielding the intermediate G30 and G60 orientations, in the G90 orientation the base curve has been oriented along the Y axis.

The plane containing the Ronchi ruling is motorized to achieve both accurate positioning of the ruling and remote motor operation, as a single central computer commands all motors. Encoder motors with 0.1-μm resolution allow for repetitive displacements along the X and the Y axes, and a stepping motor with a nominal resolution of 16 steps/deg allows for precise rotation movements of the ruling. Rotation of the ruling will be used to perform experiments with the ruling lines oriented following the X or the Y axis; both orientations of the ronchigrams will be required, owing to the lack of rotational symmetry of the samples. The need for accurate translation movements of the ruling will become evident in Subsection 3.C.

The shadow pattern created by the interaction of the wave front reflected by the sample with the Ronchi ruling (which will henceforth be called the ronchigram) is recorded by use of a CCD camera with its objective pointing at infinity. Let us denote as X (Y) ronchigrams those recorded with the ruling lines oriented following the X (Y) axis. A frame grabber located in the central computer digitizes and stores the ronchigrams as image files, which are the initial data to be processed. Note that the CCD camera is not being used to form an image of the ronchigram by focusing it onto the CCD array but just by capturing the incident wave front with its objective focused to infinity to use the CCD array as a ray slope map (see Subsection 3.B.1). This avoids the use of diffusers in the experimental setup to obtain the ronchigrams, so no speckle noise appears in the ronchigrams. As a consequence, the repetitivity of the measurements is extremely high; the rms error in successive measurements has been calculated as 2.1×10^{-4} rad in local normal measurements from successive ronchigrams under the experimental conditions described.

B. Data-Processing Operations

Starting from the stored ronchigrams, a set of well-known image-processing operations are combined with ray-tracing calculations and an integration step to yield the final profile of the surface. The relevant parameters of the surface will be obtained from the measured profile by surface fitting. The set of procedures applied to the ronchigrams is schematically depicted in Fig. 3 and briefly discussed below.

1. Initial Data Processing

One X ronchigram and one Y ronchigram are required for obtaining two-dimensional information on the non-rotationally symmetrical wave front impinging on the Ronchi ruling. Both X and Y ronchigrams are initially smoothed with 5×5 neighbor averaging to reduce the effect of ambient noise in the measurement. Pixels at the aperture edge were averaged with the values of their two closest neighbors in those directions where real data were available. The smoothed ronchigrams are then binarized with a threshold procedure. This leaves us with a set of wide bright lines where only those pixels above a certain intensity level are left active. Next, those wide lines are eroded to leave active only the central pixel line of each wide bright line, yielding what will be called the line pattern of the ronchigram.

The desired two-dimensional information on the wave front impinging on the Ronchi ruling plane is obtained by means of superimposing the line patterns

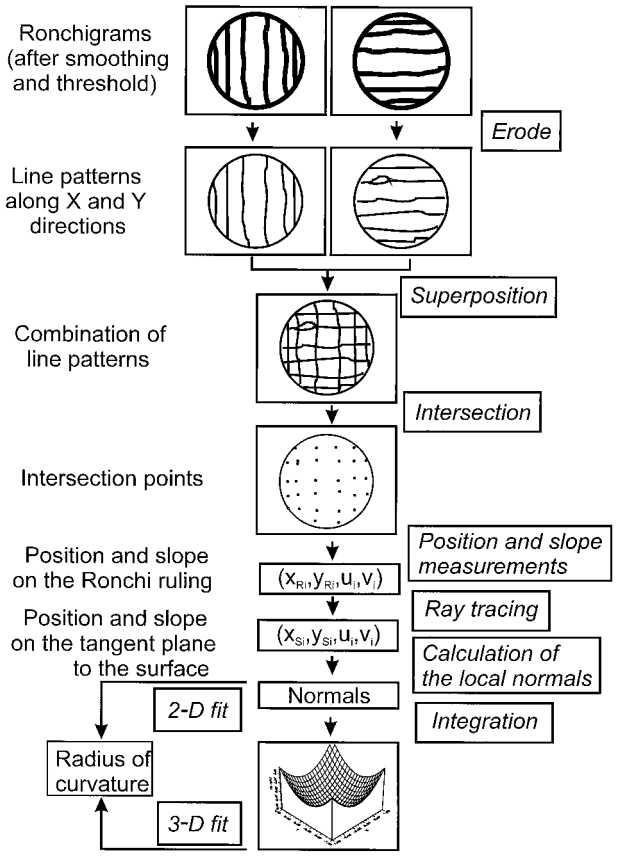

Fig. 3. Data-processing operations from the ronchigram to the surface profile. 2-D, two dimensional; 3-D, three dimensional.

obtained from the X and the Y ronchigrams. In the intersection points of both line patterns, information coming from both the X and the Y ronchigrams may be obtained.

2. *Position and Slope of the Rays at the Ronchi Ruling*

Each intersection of the line patterns obtained from the X and the Y ronchigrams provides two-dimensional information on the slope of one ray impinging on the Ronchi ruling at a certain position. The position of the intersection point i on the Ronchi ruling plane (x_{Ri}, y_{Ri}) is determined by means of the period of the ruling, on the condition that an absolute reference line be placed on the ruling. Since the ronchigram was registered with the objective of the CCD camera pointing at infinity, each pixel in the CCD array will receive those rays with a given slope. The slope of the ray impinging at the pixel (n_{Xi}, n_{Yi}) on the CCD array is

$$u_i = n_{Xi}(\Delta x/f'),$$
$$v_i = n_{Yi}(\Delta y/f'), \tag{4}$$

n_{Xi} (n_{Yi}) being the distance in pixels along the X (Y) axis from the center of the CCD array to the pixel where the considered ray impinges, Δx (Δy) the pixel size in the direction of the X (Y) axis, and f' the effective focal length of the objective. The association of the position coordinates of the intersection point obtained with the ruling pitch with the slope measurements obtained from the pixel where the intersection point has been registered in the CCD array allows us to obtain two-dimensional information on a ray reflected on the sample. A final four-number set $(x_{Ri}, y_{Ri}, u_i, v_i)$ describing a reflected ray is obtained from each intersection point arising from the superposition of the central 1-pixel-wide line patterns coming from the X and the Y ronchigrams.

3. *Position and Slope of the Rays at the Surface*

Up to this point, the two-dimensional slope and incidence position of a set of rays on the Ronchi ruling have been measured. Using this information, we may ray trace these rays backward to the surface being measured. In our setup ray tracing is a simple procedure, since no optically active surfaces are placed between the Ronchi ruling and the sample surface, except for the pellicle beam splitter. Moreover, it has been shown[17] that ray tracing to the plane tangent to the surface at its vertex or ray tracing to the real surface produces equivalent results for local normal measurements, on the condition that the light source be located close to the center of curvature of the surface, as is the case in our samples. Under this working condition, all the angles involved in the reflection are small, and the position (x_{Si}, y_{Si}) where the reflected ray left the sample surface may be determined by use of a plane-to-plane ray-tracing step (from the Ronchi ruling plane to the plane tangent to the surface at its vertex).

Although it might appear as if the sagitta physical meaning is lost with this tangent plane assumption, it should be kept in mind that the goal of our measurement is not the sagitta but the local normal value of the surface at the considered point. If the source is placed close to the center of curvature of the surface, the differences in the computed local normal value obtained by ray tracing to the real surface or to the plane tangent to the surface at its vertex may be neglected. The physical meaning of the sagitta will be recovered when the integration procedure of the set of measured local normals to the surface is performed.

As a result, the position where each ray incident on the Ronchi ruling is reflected on the sample surface (x_{Si}, y_{Si}) and the slope of the corresponding reflected ray (u_i, v_i) become known data.

4. *Local Normal Measurement*

With use of the position where the reflected ray leaves the sample surface, and the known position of the light source, the slope of the ray incident on the surface at (x_{Si}, y_{Si}) may be obtained. Once the slopes of the incident and the reflected rays are known, measuring the normal to the surface at the reflection point (the local normal to the surface) is straightforward by use of Snell's law. One local normal data value (N_{Xi}, N_{Yi}) is obtained for each of the original intersection points.

5. Integration

An iterative integration procedure is performed to yield the final profile of the surface. Each normal value is assigned to a certain sample area, depending on the number of sampling points available. For each of these areas a given height value is calculated from the corresponding local normal value and the height differences with the edges of all neighboring areas, and an inclination of the area is determined from the direction of its corresponding local normal. The process iterates until, for all sampling points, the sum of the height differences of the edges of each area with those of all its neighboring areas stays below an undetectable threshold value.

6. Measurement of the Surface Parameters

Radius-of-curvature values will be obtained from the measured data by fitting procedures. The values may be obtained prior to the integration procedure by linear fitting of the local normal against position curves along the principal meridians of the toroidal surface. When the principal meridians of the surface are oriented along the X and the Y axes (the case with orientations G00 and G90), the curves are the plots of $N_X(x_S)$ and $N_Y(y_S)$. When the principal meridians do not coincide with the X or the Y axes, a projection of the measured data must be performed to obtain the local normal slope against position values along the principal meridians of the surface, yielding what we call the $N_X{}^{\alpha}(x_S{}^{\alpha})$ and the $N_Y{}^{\alpha}(y_S{}^{\alpha})$ curves, α being the angle from the X axis where the principal meridians are oriented. This type of procedure requires either knowing *a priori* the orientation of the principal meridians of the surface or finding this orientation by iterative trials to search for the value of α at which the $N_X{}^{\alpha}(x_S{}^{\alpha})$ and the $N_Y{}^{\alpha}(y_S{}^{\alpha})$ curves have better correlation coefficients for a linear fit.

Once the integration step has been carried out and a full height profile of the surface has been obtained, an alternative method may be used to fix the parameters of the surface. We can apply a three-dimensional surface-fitting procedure by adjusting the tilted and the decentered spherocylindrical surface described in Eq. (3) to the measured height profile, allowing for the determination of the radii of the base and of the cross curves, the orientation of the principal meridians, and the position of the vertex of the surface. For these surface-fitting procedures all parameters are obtained automatically without the need for *a priori* information on the sample orientation. The differences of measured surface from the expected surface may also be calculated, showing the deviations of the surface from its ideal shape.

C. Enhancement Techniques: Microstepping

The data-processing procedure presented allows for a simple enhancement technique that enables the user to select the desired density of sampling points, within certain limits. Up to now just one X and one Y ronchigram have been acquired and processed. Under typical experimental conditions approximately ten bright lines would be visible in each of the ronchigrams. This yields an estimate of 100 sampling points on the surface when the line patterns coming from the X and the Y ronchigrams are superimposed and their intersection points calculated.

However, if nX ronchigrams and nY ronchigrams were recorded displacing the ruling a distance T/n along the direction orthogonal to the ruling lines, all the recorded ronchigrams could be processed as described in Subsection 3.B.1. The resultant $2n$ line patterns could then be superimposed to yield a pattern containing $10n$ lines along the X axis and $10n$ lines along the Y axis, thereby maintaining our estimate of ten bright lines per ronchigram. Note that the number of sampling points obtained from the intersection of the families of X and Y ronchigrams rises to $100n^2$. If 10 X ronchigrams and 10 Y ronchigrams are acquired, the number of sampling points on the surface rises by 2 orders of magnitude.

Other ruling schemes, such as the square grid of Ref. 4, do not require changing of the ruling orientation in the measurements. Although two different ruling orientations are required in our setup, the use of a square transmitance ruling allows for an important increase in the number of sampling points, which would not be achieved by a square grid scheme with a small number of displacements. In addition, the presented technique avoids the diffractive noise problem that is usual in phase-shifting techniques by ignoring the shape of the registered signal and simply considering the central position of each bright fringe. Such a geometrical approach allows for the application of microstepping techniques even in largely aberrated wave fronts, where the application of phase-shifting techniques may not be evident.

The high sampling density achieved compensates for the apparent loss in accuracy carried on by not making use of phase-shifting techniques. The closeness of the measured sampling points carries on small integration areas assigned to each local normal value (see Subsection 3.B.5), so the integration step allows for measurement of detailed surface topographies. As shown below, the topographic measurements obtained attain micrometric accuracy and are able to depict surface details with just some tenths of nanometers in depth when the deviations from the ideal shape are considered.

We called this technique microstepping, because of the micrometric nature of the stepping displacements involved. The implementation of a microstepping experiment is simple in the depicted experimental setup. With typical frequencies of the ruling of 50 lpi ($T = 0.508$ mm) the displacement of the ruling in consecutive ronchigram acquisitions to obtain ten different ronchigrams becomes 50.8 μm, a displacement available to most lab motors. It now becomes clear why in our experimental setup the Ronchi ruling plane was motorized for movement along the X and the Y axes and rotation around the Z axis. Because all the motors are controlled with a computer that already contains the frame grabber, the data-acquisition procedures become highly automated.

The microstepping procedure will also work, acquiring a different number of X and Y ronchigrams, thus allowing the user to adjust the experiment to obtain an optimum sampling of the sample surface. Sampling densities of 30 mm^{-2} have been routinely obtained in our measurements.

Obviously, there is a limit to the density of sampling points that may be obtained with this technique, since the 1-pixel-wide lines coming from ronchigrams in consecutive acquisitions are required not to overlap in order to provide reliable slope and position values after the superposition procedure. The sample area covered by the experimental setup in the measurement is also a limiting factor. However, the computing time required for managing the amount of information generated by the microstepping procedures usually becomes the most limiting factor in everyday practice, particularly if iterative integration procedures are to be carried out.

4. Experimental Results

A. Experiment

The experimental setup presented in Subsection 3.A will be used to measure the three-dimensional surface profile and to fix the radii of curvature; the orientation of the principal meridians; and the position of the vertex of a toroidal sample at the four different orientations described as G00, G30, G60, and G90 in Subsection 3.A. A binary Ronchi ruling with 50 × 50 duty ratio and a frequency of 50 lpi (T = 0.508 mm) was used, and $n = 10$ steps were applied in microstepping procedures to provide an intensive sampling of the test surface. The distance from the vertex of the surface to the Ronchi ruling was fixed at 182.6 mm in all the measurements performed.

The toroidal surface used as a sample was the concave surface of a common astigmatic spectacle lens, with its convex surface arranged to be optically inactive. To provide a reference radius of curvature for the base and the cross curves of the sample, the curves were measured with a high-precision radioscope. The reference radius values obtained for the sample amount to 170.4 ± 1 mm for the base curve and 148.8 ± 1 mm for the cross curve. Note that the difference in height in the two principal meridians, assuming a 15 mm × 15 mm sampled area, amounts to 38λ and that a profile will be obtained without the need for *a priori* hypotheses on the surface shape. The surface shape will be required only in the final fitting procedures to determine the parameters of the surface.

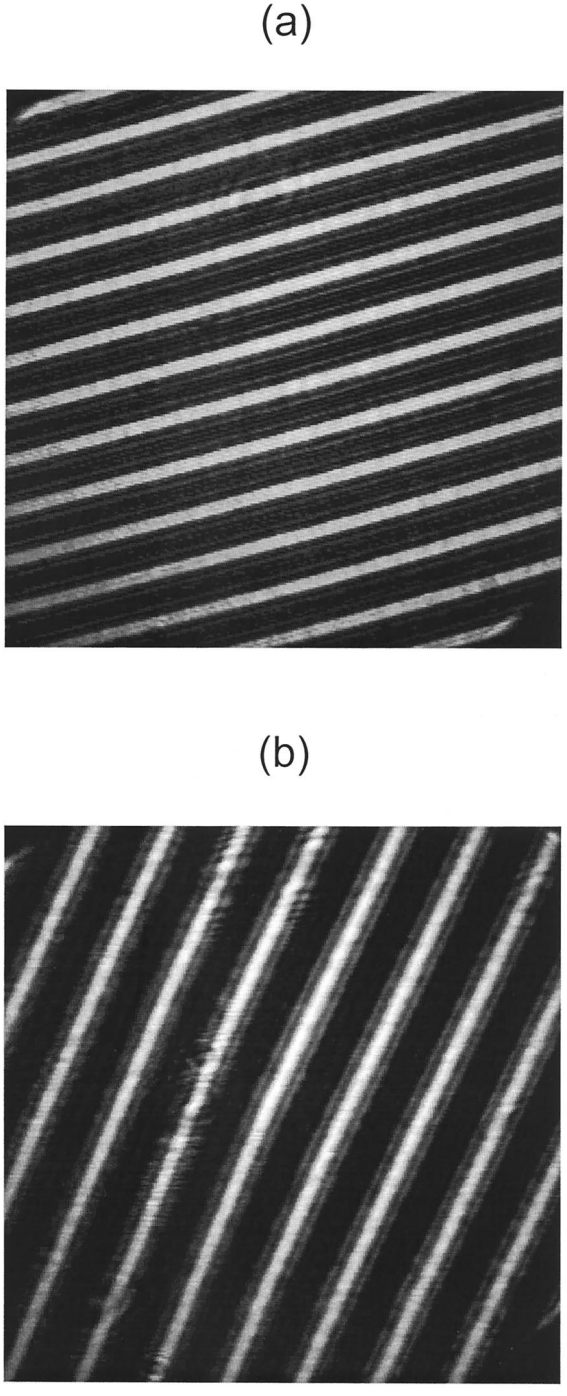

Fig. 4. Experimental ronchigrams for the sample surface: (a) X ronchigram, ruling lines placed horizontally; (b) Y ronchigram, ruling lines placed vertically.

B. Results

To provide a better understanding of the measurement technique, some of the intermediate results achieved throughout the data processing of the ronchigrams will be presented for one of the four orientations of the sample measured. We selected for this more detailed description the measurement of the sample at the G60 orientation, because in this case the principal meridians of the surface are not oriented following the direction of the lines on the ruling, showing behaviors in the ronchigrams that are never observed when the surfaces are rotationally symmetrical.

This behavior may be seen in Fig. 4, which presents the X ronchigram, where the ruling lines are placed horizontally [Fig. 4(a)], and the Y ronchigram, with the ruling lines placed vertically [Fig. 4(b)]. Note how the ronchigram lines at the presented G60 ori-

entation of the sample are not oriented in the same direction as the lines of the ruling. This is a consequence of having the principal meridians of the toroidal surface tilted from the X axis (at G60 orientation the base curve is tilted 60° from the X axis). When the Ronchi ruling lines and the principal meridians of the surface are oriented along the X and the Y axes (in the G00 or the G90 orientations), the X and the Y ronchigram lines are also oriented following the X and the Y axes, although the X and the Y ronchigrams present a different number of bright lines, owing to their different radius-of-curvature values.

A total of 10 X and 10 Y ronchigrams with their lines displaced laterally 50.8 μm ($T/10$) are acquired, smoothed, binarized, and eroded to reduce them to the set of central 1-pixel-wide lines coming from each of the bright lines on the ronchigram. The resultant 20 line patterns are superimposed to obtain the intersection points, where two-dimensional information on the slope of the rays impinging at a given position of the ruling is available. Figure 5 shows the difference between applying and not applying microstepping procedures. Whereas Fig. 5(a) is the superposition of the pair of X and Y ronchigrams presented in Fig. 4, Fig. 5(b) presents the superposition of 10 X and 10 Y microstepped ronchigrams. The number of intersection points rises from 68 in Fig. 5(a) to 7950 in Fig. 5(b), allowing for a much more intensive sampling of the surface under test. In this case the area sampled amounts to 236.8 mm^2, so the density of sampling points in the microstepped experiment is 33.6 mm^{-2}.

Through the techniques discussed in Subsection 3.B the local normal to the surface may be calculated at each of the above-mentioned 7950 sampling points. A first radius-of-curvature measurement may be performed, since along the principal meridians the local normal against position curve must be a straight line, with its slope giving the curvature of the surface. From the measured (x_{Si}, y_{Si}, N_{Xi}, N_{Yi}) values the slope against position curves along the principal meridians may be obtained through rotation, yielding the $N_X{}^{60}(x_S{}^{60})$ and $N_Y{}^{60}(y_S{}^{60})$ curves shown in Figs. 6(a) and 6(b), which correspond to the cross and the base curves of the surface, respectively. The results of fitting

$$N_J{}^{60} = C_J{}^{60}J + K_J \tag{5}$$

to the data in Fig. 6 are shown in Table 1. In Eq. (5), J may be either X or Y; C_J is the curvature along J; and K_J is the independent term, which is interpreted as an angular misalignment of the sample along the J axis. The results in Table 1 may be seen to provide an adequate fit to the reference values described for the sample. Correlation coefficients show the closeness of the measured data to a linear plot.

In addition, through integration of the local normals, one may obtain a full three-dimensional topography of the measured surface. The three-dimensional topography of the sample is presented in Fig. 7, both in the shape of a three-dimensional profile [Fig. 7(a)] and in the shape of a contour plot [Fig. 7(b)]. Whereas in the three-dimensional profile a surface has been plotted with the data, in the contour plot each plotted point is a measured sampling point on the surface, with a gray tone given by its height. Each contour step equals a 16-μm height step.

As explained in Section 2, a tilted and decentered spherocylindrical surface following Eq. (3) was fitted

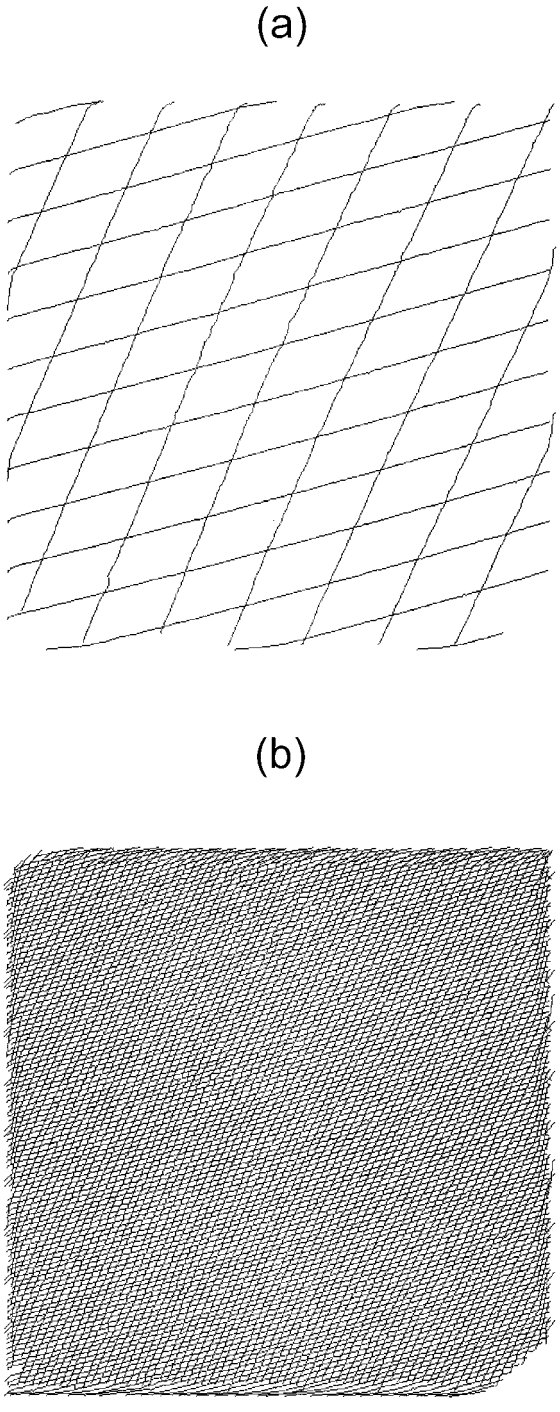

Fig. 5. Intersection of 1-pixel-wide line patterns: (a) nonmicrostepped experiment yielding 68 sampling points on the sample surface; (b) microstepped experiment yielding 7950 sampling points on the sample surface.

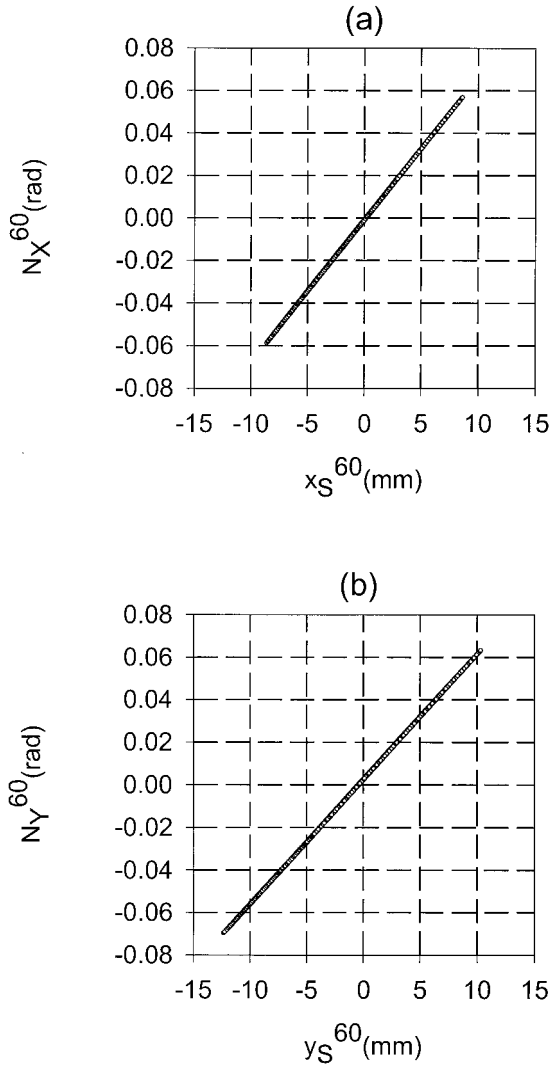

Fig. 6. G60 orientation: local normal slope against position curves along the principal meridians of the sample: (a) cross curve; (b) base curve.

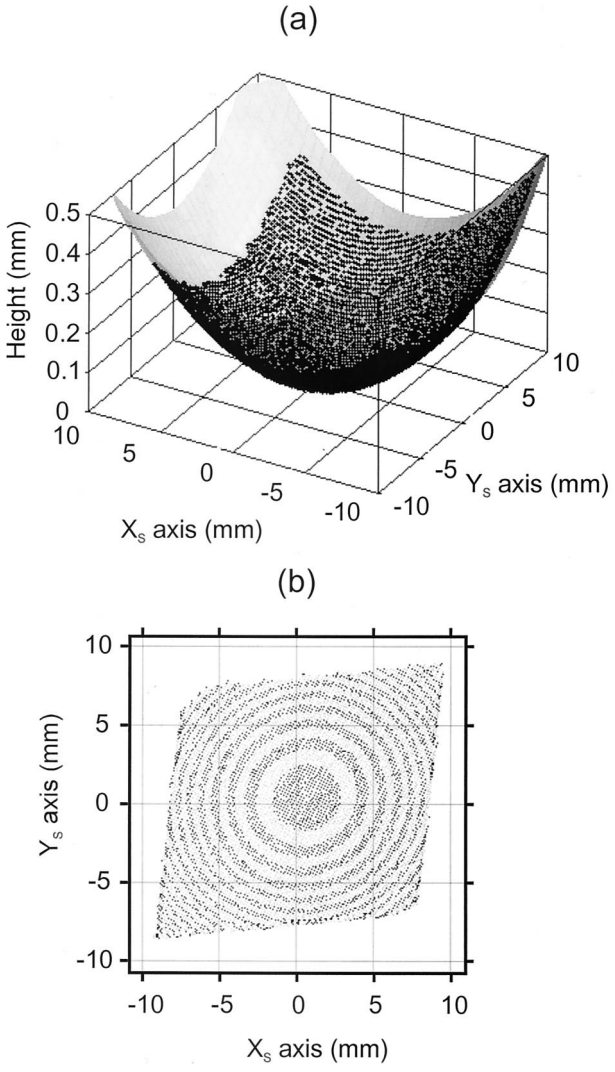

Fig. 7. G60 orientation: three-dimensional profile of the surface obtained by integration of the local normals: (a) three-dimensional plot, (b) contour plot. Each contour step equals a height step of 16 μm.

to the height data obtained for each of the sampling points to fix the parameters of the sample surface. These parameters are presented in Table 2, where the measured radii may be seen to fit the described reference values adequately. The measured orientation of the principal meridians is almost coincident with the orientation at which the sample was manually set, whereas the decentering of the sample is more important along the *X*-axis direction, as can be seen in Fig. 7(b). Note the closeness of the results for the radii obtained either from linear fitting or from three-dimensional surface fitting.

Table 3 shows the results for the sample in the three additional orientations that were tested: Radius values (through linear and surface fitting), correlation coefficients, orientation of the principal meridians, and vertex position measurements are presented. Figure 8 shows the contour plots of the measured profiles at orientations G00 [Fig. 8(a)], G30 [Fig. 8(b)], and G90 [Fig. 8(c)]. The capability of the technique of measuring the profile of the toroidal surface regardless of the orientation of its principal meridians may be observed by means of comparing the measured radius values and the principal meridian orientations with the reference values at all orienta-

Table 1. G60 Orientation: Results of Fitting the Plots in Fig. 6 to Eq. (5)

Sample[a]	Base Curve	Cross Curve
C_J (mm^{-1})	5.8045×10^{-3}	6.2219×10^{-3}
K_J (rad)	2.652×10^{-3}	-7.272×10^{-3}
R_J (mm)	170.2	149.3
r^2	0.999987	0.999984

[a] C_J stands for the curvature at the meridian considered, K_J for the independent term of the linear fit, and R_J for the radius of curvature. J may be either the base or the cross curves of the surface, and r^2 is the correlation coefficient of the linear fit.

Table 2. Orientation G60: Results of the Three-Dimensional Fitting of a Tilted and Decentered Spherocylindrical Surface (Eq. 3) to the Measured Profile

Parameter[a]	Value	Reference
R_B (mm)	170.0	170.4
R_C (mm)	149.4	148.8
θ (deg)	58.8	60
x_0 (mm)	0.45	—
y_0 (mm)	0.22	—
r^2	0.999997	—

[a]The position of the vertex was set manually, so no reference value is provided. R_B stands for the radius of the base curve, R_C for the radius of the cross curve, θ for the orientation of the principal meridians, x_0 and y_0 for the coordinates of the vertex of the surface, and r^2 for the correlation coefficient of the surface fit.

tions. Dispersion of the fitted radius values for surface fitting is lower than for linear fitting, because the estimation of the direction of the principal meridians is subject to some degree of error. The maximum dispersion in surface fitted radius values in different orientations equals an oscillation of the measured total sagitta of the tested area of 0.5 μm. This deviation in sagita measurements yields a deviation in local normal measurements smaller than the uncertainty in consecutive measurements described in Subsection 3.A, so the change in radius of curvature in different orientations stays inside the uncertainty of the measurement. The concordance in radius values obtained by linear- and surface-fitting procedures regardless of how the surface is oriented shows that the radius measurement may be carried out before or after the integration procedure with full reliability. All radius measurements may be seen to fall within the measurement uncertainty associated with the reference values, and the measured orientation of the principal meridians is consistent with the ideal orientation of the sample surface, which was fixed manually. The measurement of the position of the vertex of the surface may change from one orientation to another, since the centering of the surface was also manually set, and subsequently a small decenter

Table 3. Results for the Sample in the Three Additional Orientations Measured

Orientation[a]	G00	G30	G90
N (points)	6951	7845	6828
A (mm^2)	224.9	228.3	225.6
R_B^{LINEAR} (mm)	170.4	170.4	170.1
$r_B^{2(\text{LINEAR})}$	0.999992	0.999990	0.999991
R_C^{LINEAR} (mm)	148.9	149.1	149.6
$r_C^{2(\text{LINEAR})}$	0.999991	0.999987	0.999995
R_B^{3D} (mm)	170.2	170.2	170.3
R_C^{3D} (mm)	149.1	149.2	149.4
θ (deg)	0.7	28.9	89.3
x_0 (mm)	0.64	0.07	0.49
y_0 (mm)	0.06	−0.52	0.41
$r^{2(3D)}$	0.999998	0.999997	0.999998

[a]N stands for the number of sampling points, A for the area sampled, R_B^{LINEAR} for the radius of the base curve obtained with linear fitting, R_C^{LINEAR} for the radius of the cross curve obtained with linear fitting, $r_B^{2(\text{LINEAR})}$ and $r_B^{2(\text{LINEAR})}$ for the correlation coefficients of the linear fits for the base and the cross curves, R_B^{3D} for the radius of the base curve obtained with surface fitting, R_C^{3D} for the radius of the cross curve obtained with surface fitting, θ for the orientation of the principal meridians, x_0 and y_0 for the coordinates of the vertex of the surface, $r^{2(3D)}$ for the correlation coefficient of the surface fit.

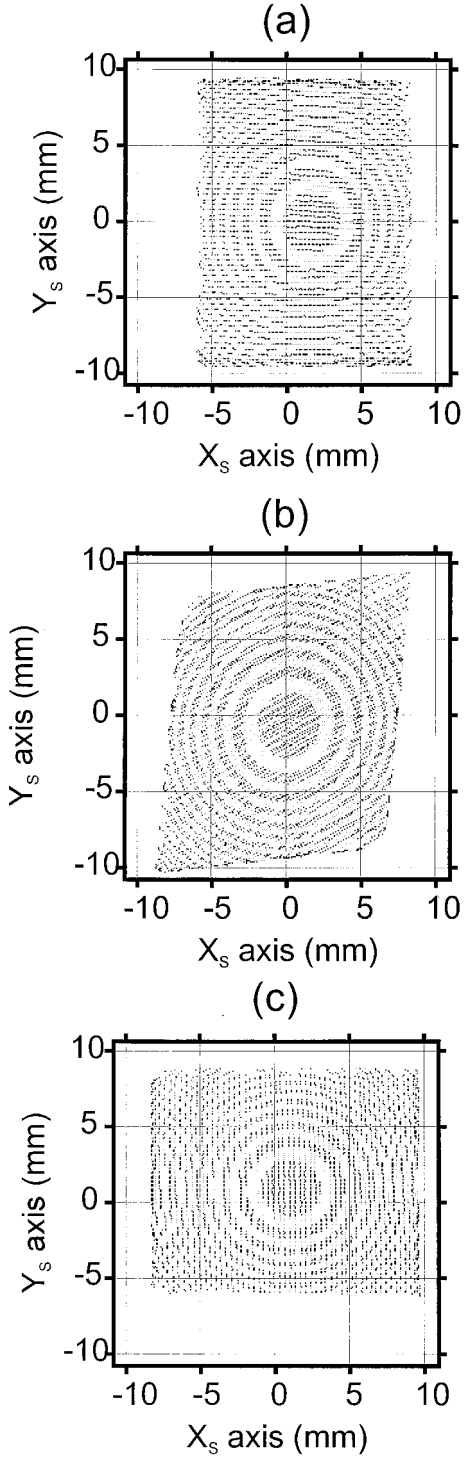

Fig. 8. Measured surface profiles, as contour plots, at the three additional orientations measured. Each contour step equals 16 μm. (a) G00 orientation, (b) G30 orientation; (c) G90 orientation.

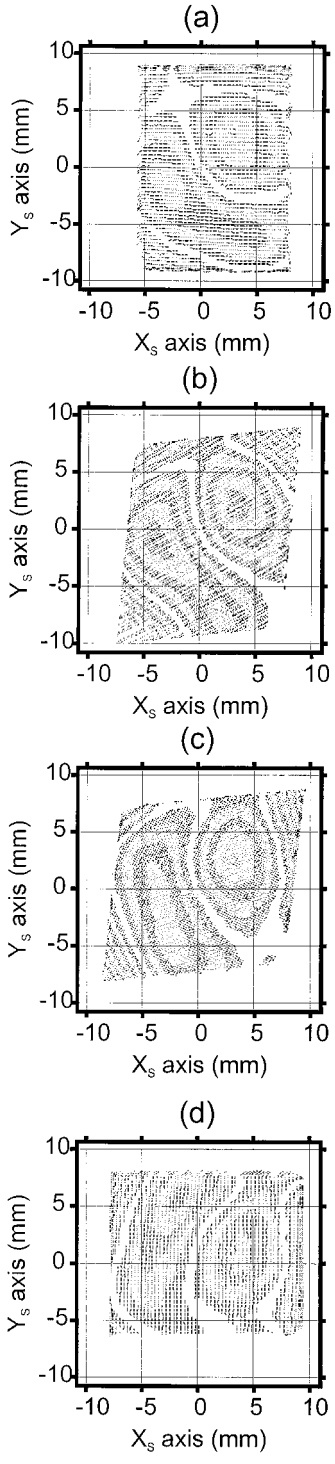

Fig. 9. Residuals obtained by subtraction of the measured profile from the best-fit profile. Each contour step equals 47 nm. (a) G00 orientation, (b) G30 orientation, (c) G60 orientation, (d) G90 orientation. Features that deviate from the ideal surface may be seen to rotate as the sample is rotated.

error is to be expected. The good correlation coefficients obtained for all the orientations considered show the closeness of the measured profile to a spherocylindrical surface.

Use of surface-fitting techniques allows us to calculate the residuals obtained when the real measured surface is subtracted from the ideally shaped spherocylindrical surface. Such plots are presented in Fig. 9. Again, a contour plot representation was performed, with the inner white contour step representing zero deviation of the measured surface from the ideal one. In this case, however, the contour step amounts to only 47 nm, so submicrometric surface details with height extensions of several tenths of nanometers are being measured for a toroidal surface. Inasmuch as the residual measurements are obtained for the same sample tilted at different orientations, the surface deviations from the ideal spherocylindrical surface may be seen to rotate as the sample rotates (note the shape and the size of the double bump at both sides of the zero contour step). The small differences in the residual plots at different orientations are due to the small radius-of-curvature differences of the fitted surfaces (see Table 3), which are subtracted from the measured surface, combined with the very small scale (47 nm) of the differences observed.

5. Conclusions

A technique based on the Ronchi test, with the capability of measuring nonrotationally symmetrical surfaces, has been presented. The experimental setup and the data-processing operations, which start with the recorded ronchigrams and end with the three-dimensional profile of the surface, have also been described. The technique has been applied to the measurement of the profile of the concave toroidal surface of a common ophthalmic lens. Additionally, a simple enhancement technique based on multiple ronchigram acquisition makes it possible to raise the density of sampling points on the measured surface to typical values of 30 mm^{-2} in the described setup.

A profile of the sample surface has been reconstructed three dimensionally without use of any *a priori* information on the shape of the surface being measured. The surface parameters (radii of curvature, orientation of the base curve, and position of its vertex) are obtained by means of surface fitting the measured height data to a spherocylindrical surface. Radius-of-curvature values may also be obtained prior to finding the topography of the surface by use of a linear fitting of the local normal against position curves along the principal meridians of the surface. Both the radii of curvature and the orientation of the meridians agree well with the reference radius values and orientations, regardless of the sample orientation and for both types of fitting procedure. Deviations from the best-fit spherocylindrical surface have been measured at different orientations, depicting surface features just some tenths of nanometers in depth.

References

1. A. Cornejo-Rodriguez, "Ronchi test," in *Optical Shop Testing*, 2nd ed., D. Malacara, ed. (Wiley, New York, 1992).
2. K. Hibino, D. I. Farrant, B. K. Award, and B. F. Oreb, "Dy-

namic range of Ronchi test with a phase-shifted sinusoidal grating," Appl. Opt. **36,** 6178–6189 (1997).
3. J. Arasa, S. Royo, and C. Pizarro, "Toroidal surface profilometries through Ronchi deflectometry: constancy under rotation of the sample," in *Applications of Photonic Technology*, G. A. Lampropoulos and R. A. Lessard, eds., Proc. SPIE **3491,** 909–915 (1998).
4. A. Cordero-Dávila, E. Luna-Aguilar, S. Vázquez-Montiel, S. Zárate-Vázquez, and M. E. Percino-Zacarías, "Ronchi test with a square grid," Appl. Opt. **37,** 672–675 (1998).
5. K. Stultz and H. P. Stahl, "A discussion of techniques that separate orthogonal data produced by Ronchi cross-grating patterns," in *Current Developments in Optical Design and Optical Engineering*, R. E. Fischer and W. J. Smith, eds., Proc. SPIE **2263,** 226–232 (1994).
6. A. Cordero-Dávila, A. Cornejo-Rodríguez, and O. Cardona-Núñez, "Ronchi and Hartmann tests with the same mathematical theory," Appl. Opt. **31,** 2370–2376 (1992).
7. A. Cordero-Dávila, A. Cornejo-Rodríguez, and O. Cardona-Núñez, "Null Hartmann and Ronchi–Hartmann tests," Appl. Opt. **29,** 4618–4621 (1990).
8. D. S. Wan and M. W. Chang, "Effects of grating spacing on the Ronchi test," Opt. Eng. **32,** 1084–1090 (1993).
9. L. Carretero, A. González, A. Fimia, and I. Pascual, "Application of the Ronchi test to intraocular lenses: a comparison of theoretical and measured results," Appl. Opt. **32,** 4132–4137 (1993).
10. W. Meyers and H. P. Stahl, "Contouring of a free oil surface," in *Interferometry: Techniques and Analysis*, G. M. Brown, O. Y. Kwon, M. Kujawinska, and G. T. Reid, eds., Proc. SPIE **1755,** 84–94 (1992).
11. K. Omura and T. Yatagai, "Phase measuring Ronchi test," Appl. Opt. **27,** 523–528 (1988).
12. H. J. Lee and S. W. Kim, "Precision profile measurement of aspheric surfaces by improved Ronchi test," Opt. Eng. **38,** 1041–1047 (1999).
13. D. Malacara and A. Cornejo, "Null Ronchi test for aspherical surfaces," Appl. Opt. **13,** 1778–1780 (1974).
14. E. Mobsby, "A Ronchi null test for paraboloids," Sky Telesc. **48,** 325–330 (1974).
15. M. Jalie, *The Principles of Ophthalmic Lenses* (Association of British Dispensing Opticians, London, 1980).
16. C. Menchaca and D. Malacara, "Toroidal and spherocylindrical surfaces," Appl. Opt. **25,** 3008–3009 (1986).
17. S. Royo, "Topographic measurements of non-rotationally symmetrical concave surfaces using Ronchi deflectometry," Ph.D. dissertation (Technical University of Catalonia, Terrassa, Spain, 1999).